Sensitivity of rip current forecasts to errors in remotely-sensed bathymetry

Radermacher, M.; de Schipper, M. A.; Reniers, A. J.H.M.

DOI
10.1016/j.coastaleng.2018.01.007

Publication date
2018

Document Version
Accepted author manuscript

Published in
Coastal Engineering

Sensitivity of rip current forecasts to errors in remotely-sensed bathymetry

M. Radermacher[a,b,*], M.A. de Schipper[a,c], A.J.H.M. Reniers[a]

[a] *Department of Hydraulic Engineering, Faculty of Civil Engineering and Geoscience, Delft University of Technology, Delft, Netherlands*
[b] *WaveDroid, Rijswijk, Netherlands*
[c] *Shore Monitoring & Research, Den Haag, Netherlands*

Abstract

Operational nearshore current forecasts based on numerical model simulations are gaining popularity as a measure to increase the safety of swimmers. Applying remotely-sensed bathymetry in these model simulations is often proposed in order to cope with rapidly changing nearshore bathymetry. Errors in the remotely-sensed bathymetry may negatively affect performance of the hydrodynamic model. Hence, this study aims to determine the sensitivity of modelled nearshore currents (with a strong focus on rip currents) to errors in remotely-sensed bathymetries.

The errors in the remotely-sensed bathymetries (depth inversion algorithm applied to video stream) were quantified with a length scale-aware validation technique, providing useful insights in the contribution of pattern and amplitude errors to the total error throughout the analysis domain and over a range of bathymetric length scales. Subsequently, simulations with a nearshore hydrodynamic model were performed, using both in-situ and remotely-sensed bathymetries as an input. A comparison of predicted rip currents on either bathymetry yielded performance statistics for operational current forecasts on remotely-sensed bathymetries, taking the model with in-situ bathymetry as a reference. Linking these performance statistics back to the quantified errors in

*Corresponding author
Email address: m.radermacher@tudelft.nl (M. Radermacher)

the remotely-sensed bathymetry finally revealed the relation between errors in flow and bathymetry.

Of all rip currents generated on an in-situ bathymetry, 55% were reproduced on the remotely-sensed bathymetry, showing that models predicting nearshore currents on remotely-sensed bathymetry have predictive value. Positive rip current predictions were promoted significantly by accurate reproduction of the pattern and amplitude of nearshore bars at length scales between 200 and 400 m. In contrast to the length-scale aware validation technique applied here, commonly used domain-wide bulk error metrics lack important information about spatial variations in the quality of remotely-sensed bathymetry.

Keywords: rip currents, depth inversion, remote sensing, Sand Motor, numerical modeling, swimmer safety

---

1. Introduction

Operational prediction of nearshore currents by numerical models is an important method for mitigation of risks related to swimmer safety (Alvarez-Ellacuria et al., 2010; Voulgaris et al., 2011; Austin et al., 2012; Kim et al., 2013; Sembiring et al., 2015). The nearshore currents predicted by these models are strongly dependent on bathymetric variability, which is most clearly illustrated by field observations of rip cell circulations related to complex sand bar patterns (MacMahan et al., 2005; Austin et al., 2010; Winter et al., 2014). In turn, these sand bar patterns are affected by nearshore hydrodynamics, as waves and currents reshape the bed continuously. Consequently, sand bar patterns that cause rip cell circulations may change drastically on timescales of days to weeks (e.g. Holman et al., 2006; Price and Ruessink, 2011). In order to reliably predict nearshore hydrodynamics for swimmer safety purposes, operational numerical models should be provided with updated bed levels frequently. This is virtually impossible to achieve with labour-intensive in-situ bed level measurement techniques (e.g. a single-beam echo sounder mounted on a personal watercraft, see MacMahan, 2001). Alternatively, nearshore bathymetry

can be estimated operationally using remote sensing techniques. The technical feasibility of coupling remotely-sensed bathymetry to nearshore hydrodynamic predictions was presented by Radermacher et al. (2014) and Sembiring et al. (2015), successfully demonstrating the potential of this combination. While they report the accuracy of the resulting simulated flow fields at their respective field sites, they do not adress the coupling between errors in the remotely-sensed bathymetry and the simulated flow fields. The aim of the present research is to determine the sensitivity of simulated rip current occurrence and location to errors in remotely-sensed bathymetries. Only geometrically defined rips related to nearshore sandbar patterns are considered. Other types of rip currents (a.o. headland rips, transient rips) are excluded here.

Over the last decades, a wide range of depth inversion algorithms has been developed, which aim to fit a local water depth to remotely-sensed wave parameters based on physical relations. For instance, these algorithms may employ wave fields observed with video or radar to estimate water depth through the linear dispersion relation (a.o. Bell, 1999; Holman et al., 2013) or model-data assimilation of video-observed wave breaking patterns (a.o. Aarninkhof et al., 2005; Van Dongeren et al., 2008). Although these remote sensing techniques are capable of providing nearshore bathymetry estimates at short time intervals, it is unclear how errors in the resulting bathymetry estimates translate to errors in the resulting flow predictions and whether the bathymetric estimates are sufficiently accurate to be applied in the prediction of nearshore hydrodynamics.

In order to be a significant contribution to recreational safety, an operational hydrodynamic model should adequately predict spatio-temporally varying nearshore current patterns. Primarily, this concerns correct prediction of rip current occurrence and location. Remotely-sensed bathymetries applied in these model simulations should be of sufficient quality to support this aim. Traditionally, the accuracy of remotely-sensed bathymetry with respect to in-situ techniques is assessed from bulk error metrics, such as the root-mean-squared error (RMSE), bias and correlation, or from difference maps (Plant et al., 2007; Senet et al., 2008; Van Dongeren et al., 2008; Holman et al., 2013; Rutten et al.,

2017). Previous attempts to assess the quality of hydrodynamic predictions on remotely-sensed bathymetry by Radermacher et al. (2014) and Sembiring et al. (2015) demonstrated the difficulty of linking bathymetric errors to hydrodynamic errors purely based on bulk point-wise error metrics. Nearshore currents do not just depend on the local water depth, but are influenced by bathymetric features that span a range of length scales (Wilson et al., 2013; Plant et al., 2009). Therefore, it is expected that the ability of a depth inversion algorithm to resolve spatial bathymetric patterns is strongly linked to the accuracy of nearshore current predictions on the remotely-sensed bathymetry.

Here, the performance of a video-based depth inversion algorithm is studied with a pattern-aware validation technique applied to the resulting bed topography maps (section 3.1). Subsequently, wave-driven nearshore currents are simulated with a validated numerical model on the remotely-sensed bathymetries and on traditionally obtained vessel-based bathymetries. A comparison of simulated flow patterns on both types of bathymetries, focused on rip currents, yields performance statistics of nearshore current predictions on remotely-sensed bathymetries (section 3.2). Finally, these current prediction performance statistics are linked to the bathymetric error statistics from section 3.1, which highlight the relation between bathymetric variability and nearshore flows (section 3.3). First, the methodology outlined above will be elaborated upon in section 2, along with a description of the study site.

2. Methodology

2.1. Field site and instrumental setup

In order to assess the accuracy of nearshore currents simulated on a video-derived bathymetry, data were obtained at the Sand Motor, a mega-scale beach nourishment in the Netherlands (Stive et al., 2013). The large scientific attention for this coastal engineering pilot project has yielded extensive field datasets (De Zeeuw et al., 2017), which have been employed here for comparison to video-derived bathymetry estimates and hydrodynamic model simulations. The Sand

Motor was constructed in 2011 as a 17.5 Mm^3 sandy peninsula and is intended to nourish the adjacent coastline throughout the coming decades by natural alongshore sediment transport. It is situated within the Delfland coastal cell, an 18 km stretch of coastline between the harbor breakwaters of Rotterdam and The Hague. At approximately two-monthly intervals, the bathymetry was surveyed (see Figure 1, panel A) with high accuracy using a single-beam echo sounder and RTK-DGPS mounted on a personal watercraft for the sub-aqueous part of the measurement domain and on an all-terrain vehicle for the sub-aerial part (details provided in De Schipper et al., 2016). The original bed elevation data were subsampled to a 25 x 25 m resolution (Plant et al., 2002) and subsequently linearly interpolated to a 20 m x 10 m grid (alongshore x cross-shore resolution). All surveys used in this study are presented in Figure 2.

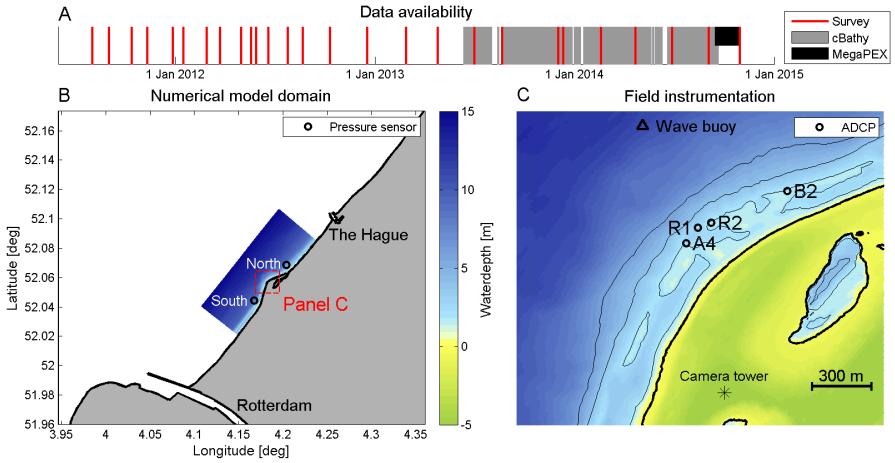

Figure 1: Overview of available field data and extent of numerical model domain: timeline of available in-situ bathymetry surveys, periods with cBathy coverage and MegaPEX experiment (panel A), position of the Sand Motor and the model domain (area covered by bathymetric data) along the Delfland coast with colours representing water depth and grey shading representing the dry land (panel B) and nearshore field setup with ADCP stations, depth contours and Argus camera tower (panel C).

An extensive set of field observations was collected in fall 2014 during the Mega Perturbation Experiment (abbreviated to MegaPEX), comprising a.o.

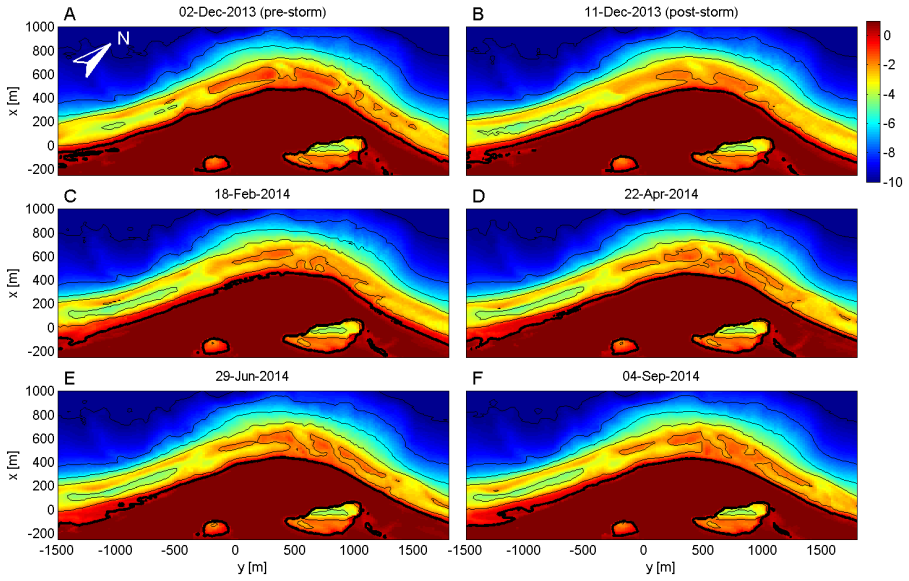

Figure 2: Overview of the six in-situ surveyed bathymetries that are used in this study. The first two surveys were captured just before and after a severe storm (peak H_s 5 m). The locations of bars and rip channels remain fairly stable, while the exact shape and orientation of bathymetric features varies throughout the analysis period. All bed levels in this study are presented relative to the Dutch vertical datum NAP (approximate mean sea level).

nearshore pressure and velocity measurements with four acoustic doppler current profilers (ADCPs) over a four-week period (Figure 1, panel C). This type of instrument has been successfully applied before for observations of nearshore current dynamics, a.o. by Brown et al. (2015). The ADCPs were deployed on the nearshore bars and at the seaward end of an oblique rip channel. They sampled the vertical current profile in bins of 0.5 m as well as the pressure. Depth-averaged flow velocities were calculated by averaging over all sub-aqueous bins (i.e. bins that are submerged more than 99% of the time within a temporal window of 10 minutes). If no sub-aqueous bins were found at a particular point in time, no depth averaged flow velocity was computed for that time. In order to remove short-term fluctuations from the timeseries, the velocity timeseries were low-pass filtered with a cut-off period of 10 minutes. Further details of the ADCPs are provided in Table 1, where h denotes the average water depth, z_{bbc}

Table 1: ADCP properties.

Station	**Type**	h **[m]**	z_{bbc} **[m]**	t_{av} **[s]**
A4	Nortek Aquadopp profiler 1 MHz	2.16	-1.18	1
R1	Nortek Aquadopp profiler 2 MHz	2.59	-1.27	15
R2	Nortek Aquadopp profiler 1 MHz	1.80	-1.15	1
B2	Nortek Aquadopp profiler 2 MHz	1.79	-1.26	20

is the vertical level of the bottom bin center and t_{av} is the internal averaging duration of the instrument. Additionally, pressure sensors were deployed at 6 m water depth just north and south of the Sand Motor.

2.2. Remotely-sensed bathymetry

A tower is located at the most elevated point of the Sand Motor, with 8 cameras covering an approximately 230 degree horizontal view angle (part of the Argus network, see Holman and Stanley, 2007). The depth inversion algorithm applied to the 2 Hz video stream is named *cBathy* (detailed description can be found in Holman et al., 2013). cBathy applies cross-spectral analysis to the video intensity timeseries in order to determine dominant pairs of frequency and wave number within a sliding spatial analysis window (Plant et al., 2008) and subsequently inverts the linear dispersion relation to make an estimate of the water depth. Timeseries of water depth estimates on a 20 x 10 m analysis grid (alongshore x cross-shore spacing) are then fed into a Kalman filter (Kalman, 1960) in order to reduce noise and make the depth estimates more robust. Applications of the cBathy algorithm to Argus imagery at various field sites and under a range of environmental conditions have demonstrated its capability to resolve nearshore bathymetry with a bulk root-mean-squared error of approximately 50 cm (Holman et al., 2013; Wengrove et al., 2013; Radermacher et al., 2014; Sembiring et al., 2015; Bergsma et al., 2016; Rutten et al., 2017). Depth estimates were obtained every four hours during daytime since installation of the camera tower in 2013, with the exception of several periods of down-time (Figure 1, panel A). For this study, cBathy's Kalman filter was initiated on 13

June 2013 and fed with 4-hourly bathymetry estimates. In addition to the algorithm presented by Holman et al. (2013), an outlier removal routine was added here to prevent several site-specific error sources (mainly ships sailing through the camera view) from fouling the remotely-sensed bathymetry. Depth estimates falling outside a 1.5 m envelope around the nearest groundtruth survey or the previous filtered bathymetry estimate were rejected. The *process error* calibration parameter was set to a value of 10^{-4} day^{-1}. This was found to yield the most accurate bathymetry estimates when compared to in-situ surveyed bed levels. It was verified that this parameter choice can cope with natural site morphodynamics by comparing cBathy results to a pre and post-storm groundtruth survey.

The present study emphasises the importance of local bathymetric patterns when studying nearshore currents. Advanced, pattern-aware comparison and verification methods for spatial parameter fields have been proposed by many authors, mostly within the field of meteorology. An extensive overview is presented by Gilleland et al. (2009). Not all methods perform equally well if the spatial parameter field consists of nearshore bed levels along a curved coastline. Scale separation methods, which assess bandpass-filtered parameter fields to perform a scale-selective comparison (e.g. Briggs and Levine, 1997), have the theoretical advantage of quantifying length scales of bathymetric patterns, but fail to separate variability due to nearshore bar patterns from variability related to the cross-shore beach profile. This is considered impractical here, as variability due to the cross-shore beach profile is irrelevant for this study of nearshore circulation patterns. The same holds for feature-based methods, which detect and compare physically relevant features by setting parameter value thresholds (e.g. Ebert and McBride, 2000).

Here, a neighborhood method is employed, which is comparable to the method presented by Bosboom and Reniers (2014). The quality of the remotely-sensed bathymetry with respect to the in-situ bathymetry is determined by computing several error metrics within a circular sliding window of diameter L. This approach acknowledges both the spatially coherent structure of the bathymetry

(by calculating bulk metrics over all points within a distance L of each other) and the spatial variability in bathymetric features encountered along a beach (by applying a sliding window over the 20 x 10 m cBathy grid). Before the error metrics are computed, the average beach slope is removed by fitting a least squares plane to the windowed in-situ bathymetry and subtracting that from both bathymetries. The error metrics were then computed as follows: let z_i be the in-situ bathymetry and z_r the remotely-sensed bathymetry within the same spatial window of n data points and z_i' and z_r' their respective counterparts after subtracting the average slope. The error metrics computed in the sliding window are (Figure 3 and Equations 1a through 1d): (1) the correlation ρ, (2) the bias b, (3) the ratio of standard deviations $\hat{\sigma}$ and (4) the root-mean-squared error ϵ.

$$\rho = \frac{\frac{1}{n}\sum_{k=1}^{n}(z_{i,k}' - \bar{z_i'})(z_{r,k}' - \bar{z_r'})}{\sigma_i \sigma_r} \tag{1a}$$

$$b = \bar{z_r} - \bar{z_i} \tag{1b}$$

$$\hat{\sigma} = \frac{\sigma_r}{\sigma_i} \tag{1c}$$

$$\epsilon = \sqrt{\frac{1}{n}\sum_{k=1}^{n}(z_{r,k} - z_{i,k})^2} \tag{1d}$$

Here, n is the number of data points inside the circular sliding window, subscripts i and r indicate in-situ or remotely-sensed quantities respectively, the overbar denotes window-averaged quantities and σ denotes the standard deviation of bed levels z' within the window.

The example shown in Figure 3 treats a spatial window with a relatively good performance of the depth inversion algorithm. The patterns are matching fairly well ($\rho = 0.93$), while the remotely-sensed bathymetry slightly underestimates the amplitude of bathymetric variability ($\hat{\sigma} = 0.96$). The bias is close to 0 and the RMSE is 0.27 cm.

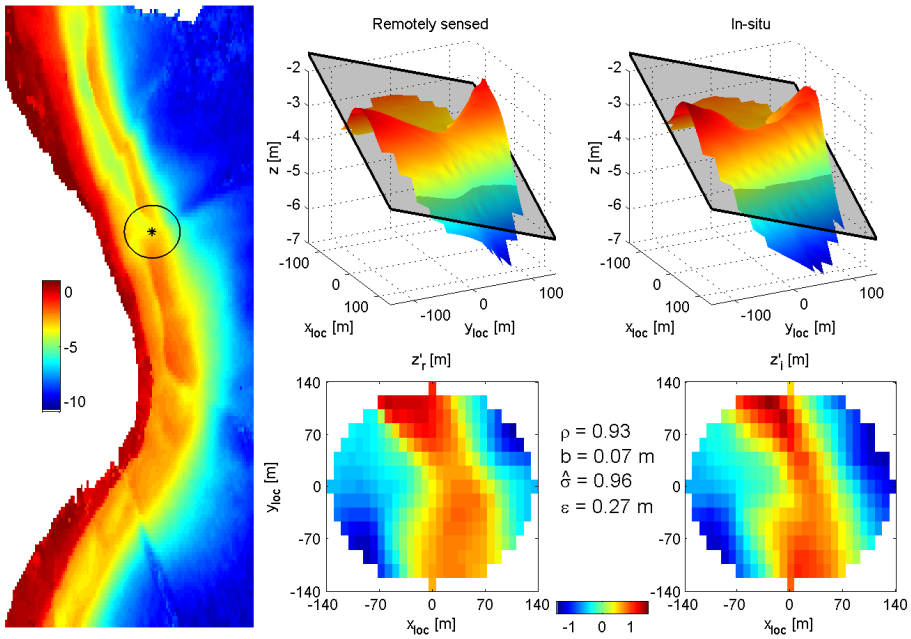

Figure 3: Demonstration of the pattern-aware bathymetry validation method. The location and size of the analysis window are indicated in the leftmost panel, along with the remotely-sensed bathymetry. The top panels show the remotely-sensed and in-situ measured bathymetries within the analysis window, including the least-squares fitted plane of the in-situ measured bathymetry. The bottom panels show the residual bathymetries z'_r and z'_i. Values of the four error metrics are stated between the bottom panels.

2.3. Numerical model

The present study relates bed level deviations in the remotely-sensed bathymetry to their impact on the nearshore flow field. To this end, nearshore currents were simulated on remotely-sensed as well as in-situ surveyed bathymetries with the Delft3D modeling suite, which has been used sucessfully for nearshore current simulation in previous studies (Elias et al., 2000; Reniers et al., 2007, 2009, 2010). The model resolves alongshore and cross-shore currents with an accuracy in the order of 10 cm/s. Setup and validation of the model are discussed in more detail in Appendix A. As the model is validated by comparing modelled flow velocities and water levels to quantities measured in the field, the

model described in the appendix is intended to closely match conditions occurring at the Delfland coast. For the simulations discussed in section 3.2, a more synthetic version of this model is applied by removing the tidal water level modulations and associated currents, as this study aims to isolate the relation between nearshore bathymetry and wave-driven currents. The wave conditions at the offshore boundary were held constant at $H_{m0} = 1.5$ m, $T_p = 6$ s and a directional spreading of 25° throughout all simulations, while the off-shore wave angle varied between simulations. The significant wave height of 1.5 m was chosen to make sure that sufficient wave energy dissipates on the subtidal bar, accounting for the generation of rip currents. The chosen wave height represents an upper limit of the wave energy that can be expected on a bright summer day at the Dutch coastline.

As studying the response of nearshore currents to nearshore bathymetry in a swimmer safety context is naturally focused on the generation of rip currents, simulated nearshore flow fields were subjected to a rip current detection algorithm. Concentrated patches of strong off-shore velocities (> 0.2 m/s) were identified as rip currents (see Figure 4 for an example). Rip current detection was performed on fields of the Generalised Lagrangian Mean flow velocity (Groeneweg and Klopman, 1998), which is resolved directly from the shallow water equations in Delft3D (Reniers et al., 2009). Following automated detection using the velocity threshold value stated above, manual quality control was performed to alleviate the discrete behavior of the rip current detection method around the velocity threshold value. The similarity of flow patterns in both simulations of a simulation pair was checked around every detected rip current. In some cases, a particular rip current was only detected in one of the two simulations, although the two simulations had visually similar flow patterns and similar off-shore velocity magnitudes. This is a result of the offshore directed flow velocity being just above and below the threshold value in the two simulations respectively. The resulting discrete behavior is considered undesirable. Therefore, automatic rip current detection in these cases was overruled by classifying both flow patterns as a rip current. Attempts to automate this correction

through quantification of flow field similarity were not successful.

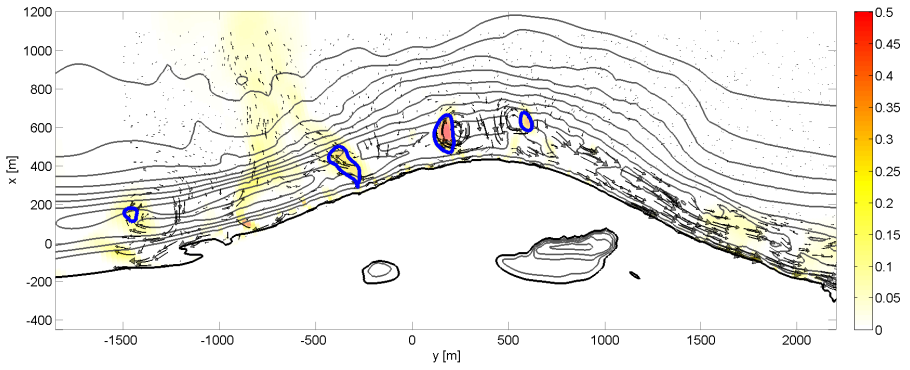

Figure 4: Example of rip current detection on computed flow field. Shading represents off-shore velocity in m/s. Four detected rip current patches have been marked in blue. The thick black line marks the 0 m bed level contour.

Subsequently, the rip current detection algorithm was applied to model simulations on six pairs of remotely-sensed and in-situ surveyed bathymetries. Each bathymetry was subjected to waves under five different off-shore angles of incidence, ranging from -30 to +30 degrees with respect to shore-normal at 15 degree intervals, constituting a total of 30 pairs of model simulations. Detected rip currents were compared between the two simulations of every pair, resulting in statistics regarding positive, false negative and false positive rip current predictions on the remotely-sensed bathymetry. For a pair of rip currents to be classified as a positive prediction, the centroids of the detected patches had to be closer than 0.75 times the sum of the alongshore patch dimensions. This criterion was found to match best with visual inspections of the similarity of simulated flow fields. The sensitivity of the results to this criterion is very small, as only 3% of all detected rip current pairs in this study are situated around the threshold value (i.e., only 3% of rip current pairs have a relative separation distance of the rip current patches between 0.5 and 1.25). A rip current predicted on the in-situ bathymetry, but not on the remotely-sensed bathymetry was counted as a false negative, while the opposite case was counted as a false positive.

3. Results

3.1. Pattern-aware validation of remotely-sensed bathymetry

Six pairs of in-situ surveyed and remotely-sensed bathymetries were subjected to the pattern-aware validation technique introduced in section 2.2. Results are treated here for the 4 September 2014 bathymetry pair as an example (see Figure 5).

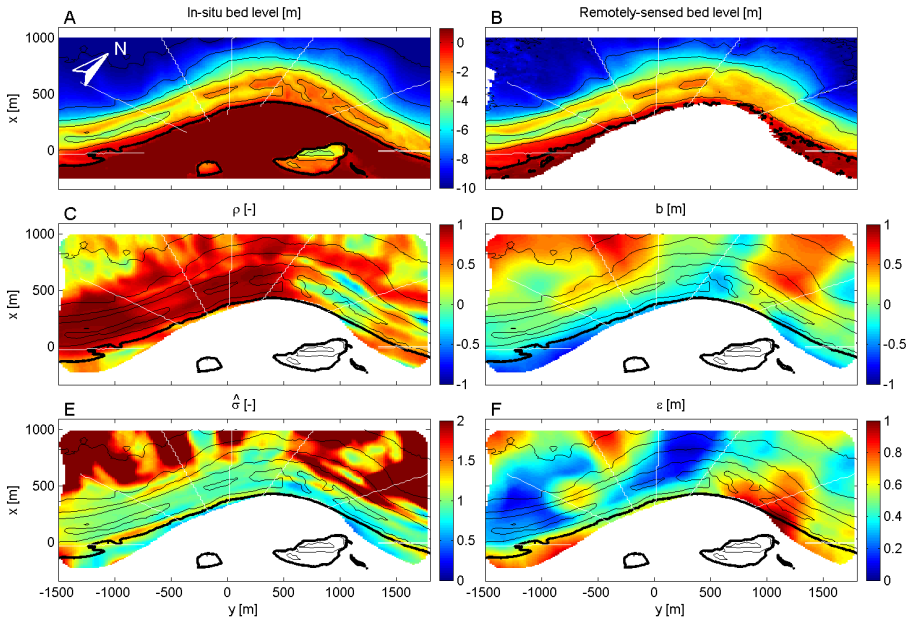

Figure 5: Bathymetric validation at 4 September 2014 with a window size L of 320 m. Panels A and B show the in-situ and remotely-sensed bathymetries, while panels C through F show the four error metrics defined in Equation 1. Bed level contours at 2m intervals were added to aid interpretation of the error metrics. Camera view boundaries are indicated as white lines.

At the scale of the entire Sand Motor, the error metrics reveal a strong divide between the southern and northern (left and right respectively in the figure) half of the nourishment on the one hand and between the nearshore and the off-shore part of the domain on the other hand. These large-scale trends are complemented with local, small-scale variations. The correlation ρ (panel C) is close to 1 along the southern edge of the Sand Motor, while it tends to 0 or

even becomes negative along the northern edge and in the off-shore corners of the domain.This mismatch of bathymetric patterns on the northern side can be confirmed by comparing panels A and B of Figure 5. In the off-shore corners, the bed is almost featureless, which allows residual noise in the remotely-sensed bathymetry to dominate the correlation.

The spatial variation in the bias b (panel D) largely confirms that the cBathy algorithm tends to underestimate the water depth at deeper waters, while it overestimates the water depth near the shoreline (also found by Holman et al., 2013; Bergsma et al., 2016; Rutten et al., 2017), although the windowed calculation reveals important local differences. Especially the sharply delineated patches of high bias in the off-shore part show that the bias at deep water differs between individual camera views. This suggests that the deep water bias can partly be explained by inadequate or outdated geo-referencing of several cameras at the Sand Motor Argus station, a problem commonly encountered at operational camera stations.

Standard deviation ratio $\hat{\sigma}$ (panel E) tends to be large in the off-shore part of the domain, while it is close to 1 in the nearshore. In the off-shore areas, as was mentioned before, residual noise in the remotely-sensed bathymetry leads to a relatively high standard deviation compared to the featureless in-situ bathymetry. The fact that $\hat{\sigma}$ is close to 1 in the nearshore areas indicates that cBathy is generally well-capable of reproducing bathymetric variability there.

Finally, the root-mean squared error (RMSE) ϵ (panel F) contains strong spatial variations. This goes to show that the bulk, domain-wide RMSE, which is often reported in depth inversion validation studies (0.58 m in this case), is not a very representative indicator of the performance of a depth inversion algorithm for the entire field site. Performance may differ strongly between particular zones in the field of view of a camera station. The windowed calculation of ϵ already gives more insight and can be regarded as an aggregated error metric that reflects the combined effect of the three other parameters (Murphy and Epstein, 1989).

A synoptic overview of these four error metrics throughout all six bathymetry

pairs can be constructed by cross-shore averaging of the error metrics over the nearshore part of the profile (between the -1 m and -5 m bed level contours, see Figure 6). Pattern-aware validation of all bathymetry pairs yields similar results regarding the large-scale contradictions in performance between the southern and northern side. At smaller scales, temporal evolution of the bathymetric quality can be observed. Especially the deterioration of ρ, b and ϵ around $y = 1000$ m from the April 2014 survey onwards is remarkable. This is related to the development from a rather featureless or cluttered bathymetry before that date to a bathymetry with well-defined bar patterns in that area. As the remotely-sensed bathymetry fails to reproduce clear bar patterns along the northern edge of the nourishment, its skill to reproduce the in-situ bathymetric patterns there (reflected by ρ) decreases sharply in April 2014.

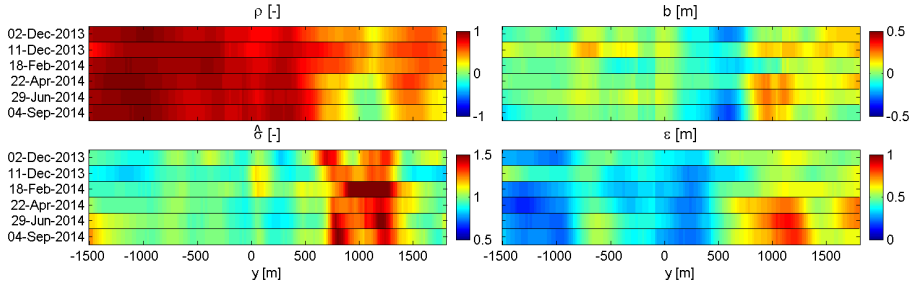

Figure 6: Nearshore-averaged error metrics for all six bathymetry pairs as a function of alongshore distance.

3.2. Nearshore current simulations

Thirty nearshore hydrodynamic model pairs with varying bathymetries and off-shore wave angles were simulated. The resulting flow fields were subjected to the rip current detection algorithm (section 2.3). Rip currents detected in pairs of model simulations were classified as positives, false negatives and false positives. The statistics over all model simulations are presented in Table 2. Out of 53 rip currents predicted on the in-situ bathymetry, 55% were positively predicted on the remotely-sensed bathymetry, while 45% of the rip currents

Table 2: Rip current prediction performance over 30 simulation pairs.

Prediction	**Occurrences**
Positive	29
False negative	24
False Positive	3

generated on an in-situ bathymetry were missed in simulations with remotely-sensed bathymetry. Out of 32 rip currents predicted on the remotely-sensed bathymetry, 9% were found to be false positive predictions that did not occur on the associated in-situ bathymetry.

It is remarkable that the number of false positives is far lower than the number of false negatives. This difference may be related to errors in the remotely-sensed bathymetry and is addressed in more detail in section 4. The map with the locations of all 56 detected rip currents throughout all simulation pairs (Figure 7) indicates that rip current formation is constrained to several rip-bar configurations in the underlying bathymetries. Most false negatives are situated along the northern edge of the nourishment, while most positives can be found around the most seaward point of the Sand Motor.

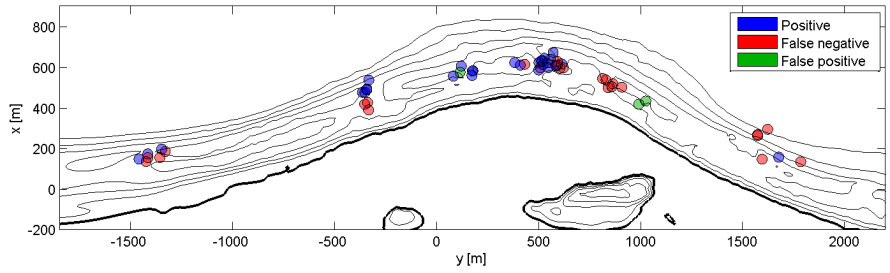

Figure 7: Overview of all detected rip currents throughout all pairs of simulations. Depth contours of the 22 April 2014 bathymetry are shown as a reference. Markers are slightly transparent to show overlapping rip currents.

3.3. Relating bathymetric errors to flow errors

In the previous section, performance statistics of simulated rip currents on remotely-sensed bathymetry were presented. The source of the input bathymetry (in-situ or cBathy) was varied between the two simulations in a simulation pair. Therefore, it is expected that observed differences between simulated flow fields and detected rip currents can (partly) be explained based on the pattern-aware bathymetry error metrics that were presented in section 3.1. For every detected rip current, the associated bathymetry errors at the center point of the rip current patch were extracted (in case of a positive rip current prediction, the mean location of the two patch centroids from both simulations was used). The bathymetric analysis length scale L was varied between 80 m and 400 m in steps of 40 m. The resulting parameters (ρ, b, $\hat{\sigma}$ and ϵ) were transformed in order to make their relation to bathymetric performance monotonous, i.e. a low parameter value means good performance and a high parameter value means bad performance, or vice versa. Parameters ρ and ϵ naturally possess this property. The absolute value was taken of b, while $\hat{\sigma}$ was transformed to $|\hat{\sigma} - 1|$. Subsequently, parameters were normalised to have zero mean and a standard deviation of 1. Normalised equivalents of the bathymetric error metrics are indicated with subscript n. Good performance is indicated by high ρ_n, low b_n, low $\hat{\sigma}_n$ and low ϵ_n.

Normalised bathymetric error metrics can now be compared for positive and false negative rip current predictions (Figure 8). False positives are omitted here due to the low number of observations (3). Bootstrapped mean parameter values and associated 95% confidence intervals per class (positive or false negative) were obtained from 10^4 realisations. The relative distance Δ between the two class averages was computed through dividing the absolute distance by half the sum of the confidence intervals of the two classes. The case $0 < \Delta < 1$ corresponds with overlapping confidence intervals of the two classes and therefore insignificant discriminative power of the associated bathymetric error metric. The case $\Delta > 1$ corresponds with non-overlapping confidence intervals and significant discriminative power.

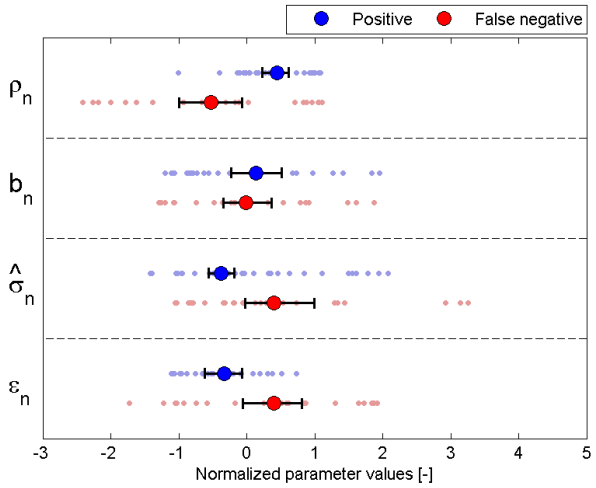

Figure 8: Normalised bathymetric error metrics for positive and false negative rip current predictions with $L = 320$ m. Bootstrapped mean values and 95% confidence intervals are presented for every parameter. Non-overlapping confidence intervals indicate discriminative power of the associated error metric, which holds for ρ_n, $\hat{\sigma}_n$ and ϵ_n.

The value of Δ has been computed for every error metric over a range of bathymetric length scales L (Figure 9). The bathymetric correlation ρ significantly differentiates between positives and false negatives for L between 200 and 400 m, the maximum value occuring at $L = 320$ m. Within this range of length scales, positive rip current predicitons are associated with significantly better correlated remotely-sensed bathymetry than false negatives. The ratio of standard deviations $\hat{\sigma}$ has significant discriminative power between $L = 240$ m and $L = 360$ m, the maximum value again occurring at $L = 320$ m. For positive rip current predictions, $\hat{\sigma}$ is significantly closer to unity (i.e. equal standard deviations and therefore equal levels of bathymetric variability) than for false negatives. The bathymetric root-mean-squared error ϵ significantly differentiates between classes for $320 < L < 400$ m, but has less discriminative strength than ρ and $\hat{\sigma}$. The bias b of the remotely-sensed bathymetry does not have a significant influence on rip current prediction performance, as Δ_b remains below unity for all tested length scales. The sharp decline of Δ for $\hat{\sigma}$ above $L = 320$ m

is remarkable, since the discriminative power of ρ and ϵ still remains significant. As L increases towards 400 m, the positive rip current predictions around the most seaward point of the nourishment start being associated with low bathymetric skill along the northern edge. Analogously, negative predictions along the northern edge start being associated with high bathymetric skill around the most seaward point. This effect, which clutters the relations between flow performance and bathymetric skill, appears to start at smaller L for $\hat{\sigma}$ than for ρ and ϵ due to differences in the spatio-temporal evolution of these parameters.

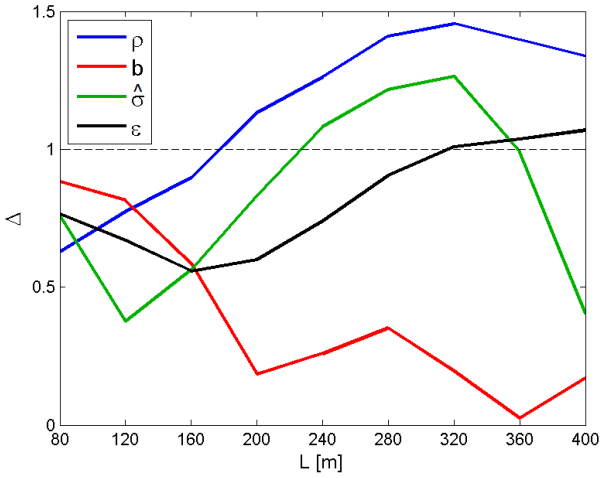

Figure 9: Relative distance Δ as a function of analysis length scale L for all bathymetric error metrics, indicating their discriminative strength.

Additionally, three flow-related parameters are examined for their discriminative strength. These parameters, being the maximum cross-shore flow velocity found in a rip current patch U, the off-shore wave angle with respect to the local shoreline orientation α and the mean alongshore flow velocity in a rip current patch V, are derived directly from the hydrodynamic simulations and therefore do not depend on L. Neither of the three selected parameters significantly differentiates between positives and false negatives, as Δ remains below unity in each case.

4. Discussion

The results presented in section 3 show that an operational rip current prediction system with updated remotely-sensed bathymetry performs best if the remotely-sensed bathymetry correlates well with the groundtruth bathymetry and if the amount of variability in both bathymetries is comparable. These relations are significant at bathymetric length scale approximately between 200 and 400 m. It implies that adequate reproduction of the pattern (related to ρ) and amplitude (related to $\hat{\sigma}$) of large nearshore sand bars by the depth inversion algorithm is most important for skilful rip current prediction. The relevant range of length scales derived here is of the same order as the scales reported by Plant et al. (2007) and Wilson et al. (2013) as the most important scales regarding cross-shore current generation. Relating length scale dependence of nearshore currents to a shallow water Reynolds number, as presented by Wilson et al. (2013), is only viable in a weakly alongshore varying regime. The presence of pronounced bathymetric variability and associated rip currents in this study hampers that approach.

False positive rip current predictions were only found in three cases, whereas false negatives are more abundant in the dataset. Because three data points are not enough to infer statistically significant relations, determining the factors promoting false positive rip current predictions based on the model simulations is difficult. However, this result may be expected based on the facts that (1) cBathy tends to overestimate nearshore water depth (e.g. Rutten et al., 2017) and (2) cBathy typically smoothens real-world bar patterns but hardly ever exaggerates bar patterns or generates non-existent bars. A positive bias of water depth in the nearshore and removal of breaker bars will promote the probability of underestimating wave breaking on the sub-tidal bar and thereby reduces bathymetric rip current forcing, leading to false negatives rather than false positives.

The numerical model simulations in the framework of this study were performed with a constant off-shore significant wave height of 1.5 m and a constant

water level equal to mean sea level. This combination of parameters was observed to induce wave breaking all along the sub-tidal bar, thereby promoting rip current generation in areas with sufficient alongshore bathymetric variability. This choice is justified by the fact that the added value of updated remotely-sensed bathymetry is primarily created by the ability to detect spatio-temporal variability in nearshore bar patterns. Whether or not rip currents are generated over a certain bathymetric pattern is mostly governed by the amount of wave energy dissipation and therefore by the ratio of the wave height at the bar crest over the local water depth, H_b/h_b. As the bar crest height varies along the coastline, progressively decreasing the off-shore wave height or increasing the (tidal) surface elevation in the numerical model simulations would lead to less and less alongshore sections with wave breaking at the sub-tidal bar. Ignoring potential dependencies between bar crest height and alongshore bathymetric variability, there is no reason to believe that a lower wave height would alter the relative performance statistics presented in Table 2. However, regarding the relations between bathymetric quality and rip current prediction identified in Figure 9, it is expected that the importance of bathymetric bias would strongly increase if the off-shore wave height is lowered. The breaker parameter for a biased bathymetry is actually $H_b/(h_b + b)$, which becomes very sensitive to the exact value of b if the breaker parameter at the bar crest is in the critical range between wave breaking and no wave breaking.

Generally, operational nearshore current prediction with video-derived bathymetry is thought to be a valuable tool for beach safety management. The present study showed that the tool has predictive value (55% positive predictions at the Sand Motor), although the exact percentage of positive predictions cannot be directly translated to other field sites. Errors in the remotely-sensed bathymetry were found to vary strongly throughout the camera domain, possibly depending on camera graze angles, geo-referencing and wave incidence angles. The Sand Motor camera station has a rather complex geometry, with a strongly curved coastline and a large area of interest. Hence, rip current prediction performance is likely to be higher along a straight coastline. Nevertheless, in day-to-day beach

safety management, numerically generated rip current predictions should always be regarded as one out of multiple information sources for lifeguards (their own experience and visual observations being other very important sources).

An important aspect of determining the merits of remotely-sensed bathymetry for rip current prediction is the trade-off between using outdated, but more accurate in-situ surveyed bathymetries or up-to-date but error-prone remotely-sensed bathymetries. The mobility of nearshore sand bar patterns plays a central role in this respect, as it determines the rate at which an outdated in-situ survey loses its power to predict the actual bathymetry. The trade-off between these two sources of bathymetry has not been addressed here, as it is outside of the scope of the present study. Recognising that an optimal prediction of up-to-date nearshore bathymetry would rely on assimilation of outdated in-situ data and up-to-date remotely-sensed data, insight in the relative accuracy of both data sources under increasing age of the in-situ data would help to determine the optimal assimilation scheme.

5. Conclusions

The present study has assessed the sensitivity of operational rip current forecasts to video-derived bathymetry estimates. It was found that rip currents predicted on remotely sensed bathymetry have predictive value. Of all rip currents generated on an in-situ bathymetry, 55% were reproduced on the remotely-sensed bathymetry. The system is prone to false negative predictions, meaning that 45% of rip currents generated on the groundtruth bathymetry are not reproduced on the remotely sensed bathymetry. In contrast, false positive predictions are rare, meaning that only 9% of rip currents predicted on the remotely sensed bathymetry do not occur on the in-situ bathymetry. This fact can be applied when using operational rip current forecasts in daily beach management, as rip currents predicted on remotely sensed bathymetry will have a very high probability of occurring in reality.

Errors in the remotely sensed bathymetry were found to exhibit strong

spatial variability due to dependence of depth inversion performance on the water depth and on camera-specific error sources (quality of the camera geo-referencing, camera resolution in real-world coordinates and alongshore differences in coastline orientation and wave incidence). Generally, depth estimates in the offshore part of the camera domain are characterised by a negative bias and a relatively high noise level, while nearshore depth estimates have a positive bias but contain realistic bar patterns (in the absense of afore-mentioned camera-specific errors sources).

The performance of rip current prediction on remotely sensed bathymetry was found to depend on the ability of the depth inversion algorithm to reproduce patterns and amplitudes of nearshore bars. Positive rip current predictions were promoted significantly by accurate reproduction of the pattern and amplitude of nearshore bars at length scales between 200 and 400 m. The angle of wave incidence, cross-shore rip current intensity and strength of the alongshore flow velocity did not significantly influence rip current prediction performance.

The results presented here imply that spatio-temporal maps of the pattern and amplitude errors of remotely-sensed bathymetry can be used to predict the performance of nearshore circulations simulated on that bathymetry. In contrast, domain-wide bulk error metrics lack important information about spatial variations in the quality of remotely-sensed bathymetry.

Acknowledgements

MR was supported by STW Grant 12686: Nature-driven Nourishments of Coastal Systems (NatureCoast), S1: Coastal safety. MdS was supported by the ERC-Advanced Grant 291206 - Nearshore Monitoring and Modeling (NEMO). We express our gratitude to the colleagues who helped us out in the field: Sierd, Bonnie, Meagan, Martijn, Bas, Marion, Wilmar, Duong, Nick and Caroline. Sierd de Vries, Greg Wilson, Wiebke Jäger, Rob Holman and Bas Huisman are thanked for their suggestions and fruitful discussions regarding this study. Rijkswaterstaat and Jamie MacMahan of the Naval Postgraduate School are

gratefully acknowledged for the use of their instrumentation in the MegaPEX campaign.

References

Aarninkhof, S.G.J., Ruessink, B.G., Roelvink, J.A., 2005. Nearshore subtidal bathymetry from time-exposure video images. Journal of Geophysical Research 110, C06011. URL: http://doi.wiley.com/10.1029/2004JC002791, doi:10.1029/2004JC002791.

Alvarez-Ellacuria, A., Orfila, A., Olabarrieta, M., Medina, R., Vizoso, G., Tintor, J., 2010. A nearshore wave and current operational forecasting system. Journal of coastal research 26, 503–509.

Austin, M.J., Scott, T.M., Brown, J., MacMahan, J., Masselink, G., Russell, P.E., 2010. Temporal observations of rip current circulation on a macro-tidal beach. Continental Shelf Research 30, 1149–1165.

Austin, M.J., Scott, T.M., Russell, P.E., Masselink, G., 2012. Rip current prediction: development, validation and evaluation of an operational tool. Journal of Coastal Research 29, 283–300.

Bell, P.S., 1999. Shallow water bathymetry derived from an analysis of x-band marine radar images of waves. Coastal Engineering 37, 513–527.

Bergsma, E.W.J., Conley, D.C., Davidson, M.A., O'Hare, T.J., 2016. Video-based nearshore bathymetry estimation in macro-tidal environments. Marine Geology 374, 31–41.

Booij, N., Ris, R.C., Holthuijsen, L.H., 1999. A third-generation wave model for coast regions: 1. Model description and validation. Journal of Geophysical Research 104, 7649–7666.

Bosboom, J., Reniers, A.J.H.M., 2014. Scale-selective validation of morphodynamic models, in: Lynett, P.J. (Ed.), Proceedings of 34th Conference on Coastal Engineering, Seoul, South Korea.

Brander, R.W., 1999. Field observations on the morphodynamic evolution of a low-energy rip current system. Marine Geology 157, 199–217.

Briggs, W.M., Levine, R.A., 1997. Wavewave and field forecast verification. Monthly Weather Review 125, 1329–1341.

Brown, J., MacMahan, J., Reniers, A., Thornton, E., 2015. Field observations of surf zone-inner shelf exchange on a rip-channeled beach. Journal of Physical Oceanography 45, 2339–2355.

De Schipper, M.A., De Vries, S., Ruessink, B.G., De Zeeuw, R.C., Rutten, J., Van Gelder-Maas, C., Stive, M.J.F., 2016. Initial spreading of a mega feeder nourishment: Observations of the Sand Engine pilot project. Coastal Engineering 111, 23–38.

De Zeeuw, R., De Schipper, M., De Vries, S., 2017. Sand motor topographic survey, actual surveyed path. doi:10.4121/uuid:3836e5a5-4fdf-4122-84bd-a9bb679fb84c.

Ebert, E.E., McBride, J.L., 2000. Verification of precipitation in weather ssystem: determination of systematic errors. Journal of Hydrology 239, 179–202.

Elias, E., Walstra, D., Roelvink, J., Stive, M., Klein, M., 2000. Hydrodynamic validation of delft3d with field measurements at egmond, in: Proceedings of ICCE 2000.

Gilleland, E., Ahijevych, D., Brown, B.G., Casati, B., Ebert, E.E., 2009. Intercomparison of spatial forecast verification methods. Weather and Forecasting 24, 1416–1430.

Groeneweg, J., Klopman, G., 1998. Changes of the mean velocity profiles in the combined wave-current motion described in a glm formulation. Journal of Fluid Mechanics 370, 271–296.

Holman, R., Plant, N., Holland, T., 2013. cBathy: A robust algorithm for estimating nearshore bathymetry. Journal of Geophysical Research: Oceans 118,

2595–2609. URL: http://doi.wiley.com/10.1002/jgrc.20199, doi:10.1002/jgrc.20199.

Holman, R.A., Stanley, J., 2007. The history and technical capabilities of argus. Coastal Engineering 54, 477–491.

Holman, R.A., Symonds, G., Thornton, E.B., Ranasinghe, R., 2006. Rip spacing and pesistence on an embayed beach. Journal of Geophysical Research: Oceans 111.

Kalman, R.E., 1960. A New Approach to Linear Filtering and Prediction Problems. Journal of Basic Engineering 82, 35–45.

Kim, I.C., Lee, J.I., Lee, J.Y., 2013. Verification of rip current simulation using a two-dimensional predictive model, haecum, in: Proceedings 12th International Coastal Symposium (Plymouth, England).

Lesser, G.R., Roelvink, J.A., Van Kester, J.A.T.M., Stelling, G.S., 2004. Development and validation of a three-dimensional morphological model. Coastal Engineering 51, 883–915.

MacMahan, J.H., 2001. Hydrographic surveying from personal watercraft. Journal of Surveying Engineering 127, 12–24.

MacMahan, J.H., Thornton, E.B., Stanton, T.P., Reniers, A.J., 2005. RIPEX: Observations of a rip current system. Marine Geology 218, 113–134. doi:10.1016/j.margeo.2005.03.019.

Murphy, A., Epstein, E., 1989. Skill scores and correlation coefficients in model verification. Monthly Weather Review 117, 572–581.

Plant, N., Holland, K., Haller, M., 2008. Ocean Wavenumber Estimation From Wave-Resolving Time Series Imagery. IEEE Transactions on Geoscience and Remote Sensing 46, 2644–2658. URL: http://ieeexplore.ieee.org/lpdocs/epic03/wrapper.htm?arnumber=4599199, doi:10.1109/TGRS.2008.919821.

Plant, N.G., Aarninkhof, S.G.J., Turner, I.L., Kingston, K.S., 2007. The performance of shoreline detection models applied to video imagery. Journal of Coastal Research 233, 658–670.

Plant, N.G., Edwards, K.L., Kaihatu, J.M., Veeramony, J., Hsu, L., Holland, T.K., 2009. The effect of bathymetric filtering on nearshore process model results. Coastal Engineering 56, 484–493.

Plant, N.G., Holland, K.T., Puleo, J.A., 2002. Analysis of the scale of errors in nearshore bathymetric data. Marine Geology 191, 71–86.

Price, T.D., Ruessink, B.G., 2011. State dynamics of a double sansand system. Continental Shelf Research 31, 659–674.

Radermacher, M., De Schipper, M.A., Swinkels, C., MacMahan, J.H., Reniers, A.J.H.M., 2017. Tidal flow separation at protruding beach nourishments. Journal of Geophysical Research: Oceans 122, 63–79.

Radermacher, M., Wengrove, M., Van Thiel De Vries, J., Holman, R., 2014. Applicability of video-derived bathymetry estimates to nearshore current model predictions. Journal of Coastal Research 66. doi:10.2112/SI65-xxx.1.

Reniers, A., MacMahan, J., Beron-Vera, F., Olascoaga, M., 2010. Rip-current pulses tied to lagrangian coherent structures. Geophysical Research Letters 37.

Reniers, A., MacMahan, J., Thornton, E., Stanton, T., 2007. Modeling of very low frequency motions during ripex. Journal of Geophysical Research 112.

Reniers, A.J.H.M., MacMahan, J.H., Thornton, E.B., Stanton, T.P., Henriquez, M., Brown, J.W., Brown, J.A., Gallagher, E., 2009. Surf zone surface retention on a rip-channeled beach. Journal of Geophysical Research 114.

Roelvink, J.A., 1993. Dissipation in random wave groups incident on a beach. Coastal Engineering 19, 127–150.

Rutten, J., De Jong, S.M., Ruessink, G., 2017. Accuracy of nearshore bathymetry inverted from X-band radar and optical video data. IEEE Transactions on Geoscience and Remote Sensing 55, 1106–1116.

Sembiring, L., Van Ormondt, M., Van Dongeren, A., Roelvink, D., 2015. A validation of an operational wave and surge prediction system for the dutch coast. Natural Hazards and Earth System Sciences 15, 1231–1242.

Senet, C.M., Seemann, J., Flampouris, S., Ziemer, F., 2008. Determination of bathymetric and current maps by the method DiSC based on the analysis of nautical X-band radar image sequences of the sea surface. IEEE Transactions on Geoscience and Remote Sensing 46, 2267–2279.

Stive, M.J.F., Schipper, M.A.D., Luijendijk, A.P., Aarninkhof, S.G.J., Geldermaas, C.V., Vries, J.S.M.V.T.D., Vries, S.D., Henriquez, M., Marx, S., Ranasinghe, R., 2013. A New Alternative to Saving Our Beaches from Sea-Level Rise: The Sand Engine. Journal of Coastal Research 29, 1001–1008. doi:10.2112/JCOASTRES-D-13-00070.1.

Svendsen, I.A., 1984. Wave heights and set-up in a surf zone. Coastal Engineering 8, 303–329.

Uittenbogaard, R.E., Van Vossen, B., 2003. Subgrid-scale model for quasi-2d turbulence in shallow water, in: Uijttewaal, W.S.J., Jirka, G.H. (Eds.), Research presented at the international symposium on shallow flows, Taylor & Francis, Delft, Netherlands.

Van Dongeren, A.R., Plant, N.G., Cohen, A., Roelvink, J.A., Haller, M.C., Catalan, P., 2008. Beach Wizard: nearshore bathymetry estimation through assimilation of model computations and remote observations. Coastal Engineering 55, 1016–1027.

Voulgaris, G., Kumar, N., Warner, J.C., 2011. Prediction of rip currents using a three-dimensional numercal, coupled, wave current model, in: Leatherman,

S., Fletemeyer, J. (Eds.), Rip Currents: Beach Safety, Physical Oceanography, and Wave Modeling, CRC Press. pp. 87–105.

Wengrove, M.E., Henriquez, M., De Schipper, M.A., Holman, R.A., Stive, M.J.F., 2013. Monitoring morphology of the Sand Engine leeside using Argus' cBathy, in: Proceedings of Coastal Dynamics 2013, Archachon, France.

Wilson, G.W., Özkan-Haller, H.T., Holman, R.a., 2013. Quantifying the length-scale dependence of surf zone advection. Journal of Geophysical Research: Oceans 118, 2393–2407. URL: http://doi.wiley.com/10.1002/jgrc.20190, doi:10.1002/jgrc.20190.

Winter, G., Van Dongeren, A.R., De Schipper, M.A., van Thiel de Vries, J., 2014. Rip currents under obliquely incident wind waves and tidal longshore currents. Coastal Engineering 89, 106–119. URL: http://linkinghub.elsevier.com/retrieve/pii/S0378383914000635, doi:10.1016/j.coastaleng.2014.04.001.

Appendix A. Numerical model

Appendix A.1. Numerical model setup

A hydrodynamic model of the Sand Motor was constructed with the modeling suite Delft3D (Lesser et al., 2004), which numerically integrates the shallow water equations. Forcing of the flow by waves was taken into account by solving the wave action balance with the SWAN model (Booij et al., 1999). The main model domain (flow and waves) covers an area of 9.4 x 4.0 km (alongshore x cross-shore) and has a curvi-linear grid that follows the coastline orientation. The spatial extent of the grid is equal to the shaded area in panel B of Figure 1. The wave model was nested in a coarse, rectangular model grid with a larger alongshore extent to account for realistic boundary conditions along the lateral boundaries of the detailed model. A grid resolution of 5 m was adopted in the nearshore area in order to accurately represent wave breaking and forcing of wave-driven currents. The time step for numerical integration was 6 seconds.

Tidal currents were forced by varying water levels imposed at the off-shore model boundary. Water level data were obtained from pressure sensors at 6 m water depth, which have been corrected for changes in athmospheric pressure and low-pass filtered with a cut-off period of 15 minutes. A tidal water level gradient was superimposed in alongshore direction, based on gradients predicted by the continental shelf model and nested coastal strip model (Sembiring et al., 2015), which propagate the astronomical tide from the edge of the European continental shelf to the Dutch coast. This approach was shown to yield accurate tidal currents in the shallow coastal waters around the Sand Motor (Radermacher et al., 2017). Neumann boundary conditions were imposed at the lateral boundaries of the flow model. Friction was specified with the Chzy formulation and a friction coefficient of 50 $m^{1/2}/s$. Horizontal Large Eddy Simulation (HLES, Uittenbogaard and Van Vossen, 2003) was applied for turbulence closure, providing spatially and temporally varying turbulent viscosities with an averaging duration of 30 minutes and a background viscosity of 0.01 m^2/s.

Parametric boundary conditions for the largest wave grid were obtained from a nearshore waverider buoy at 11 m depth just north of the Sand Motor. Wave conditions were corrected for shoaling and refraction and shifted in time to represent conditions at the off-shore model boundary. Depth-induced wave breaking was accounted for by a combination of the wave energy dissipation formulation by Roelvink (1993) and a roller energy balance (Svendsen, 1984) with breaker parameter $\gamma = 0.8$ and roller slope $\beta = 0.1$.

This model setup is very similar to the approach of Reniers et al. (2007), Reniers et al. (2009) and Reniers et al. (2010), who successfully demonstrated the capability of the Delft3D suite to model nearshore current dynamics.

Appendix A.2. Comparison to field observations

Calculated wave and flow parameters are now compared to quantities observed in the field over a 6-day period in early October 2014 (Figure A.10). Over this period, the wave energy was relatively high and the wave height peaked twice at approximately 1.5 m. This gave rise to distinct wave-driven currents

in the nearshore, which makes it a relevant period for model-data comparison in the light of operational forecasts of potentially hazardous currents.

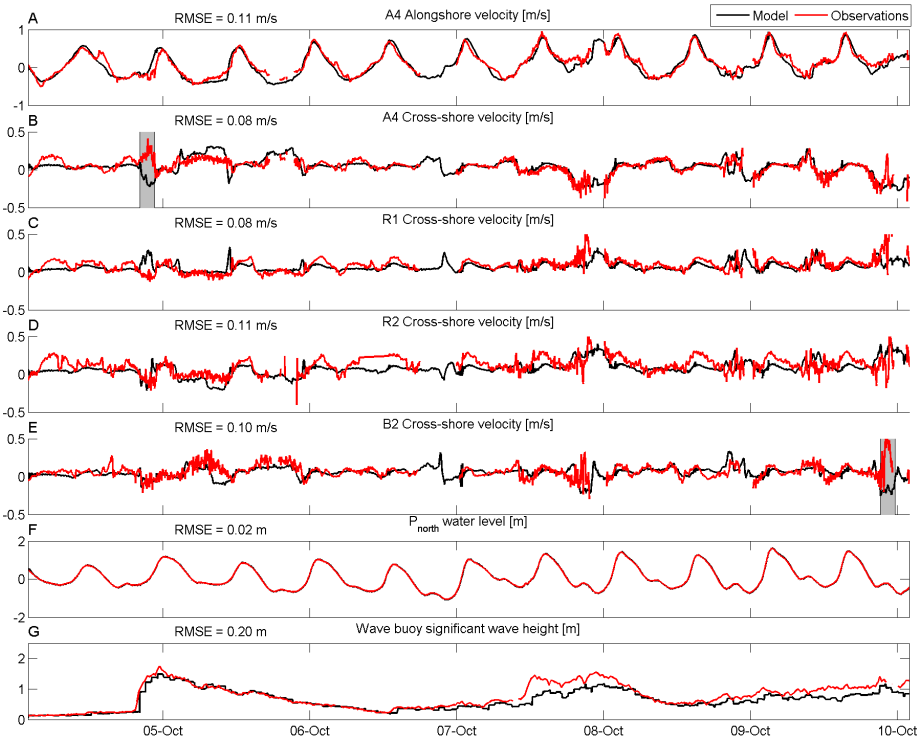

Figure A.10: Comparison of measured (red) and computed (black) flow and wave quantities. The panels show the depth-averaged alongshore velocity component (panel A), depth-averaged cross-shore velocity component (panels B-E), water level (panel F) and significant wave height (panel G) at various measurement stations. Shaded periods in panels B and E are analysed in more detail.

Alongshore currents observed in the field (panel A of Figure A.10) are mostly dominated by the semi-diurnal tidal currents, with positive currents corresponding to flood flow in northeastern direction. Around the second wave energy peak at 7 October, which had more oblique southwesterly waves than the first peak, alongshore wave-driven currents can be seen to dominate the alongshore velocity signal. The numerical model is well-capable of resolving alongshore currents, with very similar performance across all ADCP stations.

Cross-shore currents (panels B-E) exhibit more variability between different stations. During calm conditions, separation of the tidal flow and creation of large-scale tidal eddies causes slight tidal modulations of the cross-shore flow velocity (see Radermacher et al., 2017, for a more elaborate analysis of tidal currents around the Sand Motor). The two wave energy peaks drive more intense cross-shore currents. The maximum wave height is similar during both peaks, but the first peak is observed to drive less intense cross-shore currents as it coincides with high water. This leads to less intense wave breaking on the subtidal bars and consequently to weaker forcing of nearshore circulations (e.g. Brander, 1999). The modelled cross-shore currents are in reasonable agreement with the field observations, especially in the second half of the comparison period. Differences are in part attributed to schematisations in the modelling approach, but may also result from slight spatial shifts of modelled flow patterns. The latter is illustrated by a comparison of computed flow fields around ADCP locations A4 and B2 during two events with strong cross-shore currents (Figure A.11).

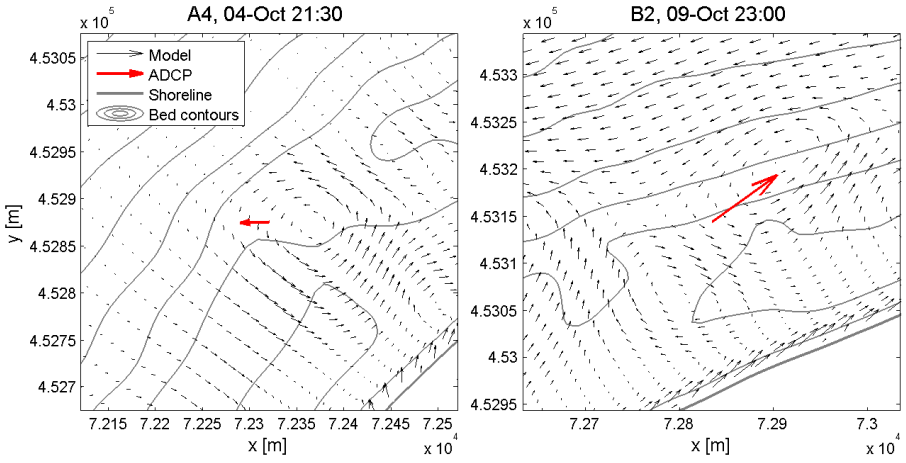

Figure A.11: Computed flow fields and observed local flow velocities at A4 and B2 during two events with strong cross-shore currents.